Ceramics International xxx (xxxx) xxx

Contents lists available at ScienceDirect

Ceramics International

journal homepage: www.elsevier.com/locate/ceramint

Wear-resistant HfC_x film with infrared-visible compatible stealth property

Gaopeng Zou [a], Qianqian Wang [a,b,*], Ruixin Sheng [a], Ligang Sun [c,**], Qiyue Shao [a], Xuhai Zhang [a], Zhe Jia [a], Baolong Shen [a,***]

[a] School of Materials and Engineering, Jiangsu Key Laboratory for Advanced Metallic Materials, Southeast University, Nanjing, 211189, China
[b] School of Materials Science and Engineering, Jiangsu Key Laboratory of Advanced Structural Materials and Application Technology, Nanjing Institute of Technology, Nanjing, 211167, China
[c] School of Science, Harbin Institute of Technology, Shenzhen, 518055, China

ARTICLE INFO

Handling Editor: Dr P. Vincenzini

Keywords:
HfC_x film
C stoichiometry
Energy input
Infrared-visible compatible stealth
Wear-resistance

ABSTRACT

Ultra-high temperature ceramic films have offered a combination of low infrared emissivity and durability in extremely harsh environments. However, desired applications have been limited by high visible light reflectivity. Herein, a novel strategy, by adjusting C stoichiometry and energy input, is proposed to construct a $HfC_{0.91}$ film consisted of HfC columnar nanograins with a width of 14.3 ± 0.4 nm and a-C phase at triple junctions, as well as exhibiting significantly increased surface roughness. The resulting microstructure simultaneously achieved excellent infrared-visible compatible stealth and tribo-mechanical properties. The infrared reflectivity/emissivity in the wavelength band of 8–14 μm is 0.9/0.1 primarily attributed to a reduction in lattice vibration absorption, while the low visible reflectivity (0.33) is mainly dominated by reduced plasma energy and enhanced multiple scattering absorption. Furthermore, the $HfC_{0.91}$ film exhibited improved wear-resistance due to the self-lubricating properties of a-C phase. Thus, this work offers a new strategy for designing wear-resistant HfC_x film with infrared-visible compatible stealth property for application in extreme thermo-mechanical service environments.

1. Introduction

For most of the military targets, the ability to evade from infrared detectors significantly enhances their survivability and striking effectiveness on the battlefield [1]. Infrared stealth technology, which aims to minimize the infrared radiation differences between a target and its surroundings by reducing the temperature or the emissivity of the targets surface based on the Stefan-Boltzman's law, reduces the risk of detection by infrared detectors, making it crucial for national defense security [2–7]. Depositing low infrared emissivity film on the target surface is an effective strategy for achieving infrared stealth and has garnered significant attention.

Numerous studies have demonstrated that metal films (e.g., Pt [8], Ag [9], Au [10]) exhibit excellent infrared stealth performance. However, these films possess low mechanical properties and exhibit poor environmental stability, making them susceptible to wear and oxidation in harsh battlefield environments, which ultimately compromises their infrared stealth capabilities. In order to improve durability of these metal films, transparent oxide ceramic layers, such as SiO_2 [11] and Al_2O_3 [12], are usually applied on top to protect them from environment damage. Unfortunately, this strategy has limitations as the hard protection layer needs to be reduced to a few dozen nanometers in thickness to avoid reflectivity loss and delamination [13]. In addition, as metal films possess high visible reflectivity, they can be easily detected by visible detectors [14,15]. These shortcomings restrict the wide application of metal films.

To obtain infrared-visible (IR-vis) compatible stealth characteristics, various approaches have been reported, including preparing nano-multilayer films [6,16–18] and metamaterials [19–23]. For instance, Deng et al. [6] developed a nanostructured film comprised of a Ge/ZnS multilayer mounted with nanolayered dielectric antireflection stacks, which were characterized by low visibility and low thermal emission. In this nanostructure, the Ge/ZnS multilayer served to suppress thermal emission, while the antireflection stacks were designed to absorb visible

* Corresponding author. School of Materials and Engineering, Jiangsu Key Laboratory for Advanced Metallic Materials, Southeast University, Nanjing, 211189, China.
** Corresponding author.
*** Corresponding author.
E-mail addresses: qwang678@seu.edu.cn (Q. Wang), sunligang@hit.edu.cn (L. Sun), blshen@seu.edu.cn (B. Shen).

https://doi.org/10.1016/j.ceramint.2025.04.052
Received 15 November 2024; Received in revised form 3 April 2025; Accepted 5 April 2025
Available online 7 April 2025

light. Xiong et al. [23] obtained a multispectral camouflage metamaterial by electrochemically fabricating porous aluminum oxide (AAO) as the dielectric layer and depositing a thin metal film by direct current ion sputtering technique as plasmonic absorption layer. This configuration effectively generates color for visible camouflage and low infrared emissivity for infrared camouflage. However, such nanostructures require complex fabrication techniques with nanoscale precision, making them difficult and costly to scale. IR-vis compatible stealth films with simple structure, excellent mechanical properties and environmental stability needs to be developed.

Recently, transition metal nitrides (TMNs) and borides (TMBs), such as HfN [13] and ZrB_2 [15,24,25], have emerged as promising infrared stealth film materials for harsh environments. These TMNs and TMBs exhibit low emissivity in infrared bands, along with exceptional hardness and thermal stability. For instance, Zhang et al. [25] reported that ZrB_2 thin films maintain a low infrared emissivity of 0.01 (8–14 μm) even after annealed at 1000 °C for 10 h. Hu et al. [13] observed that Ag-doped HfN film displayed a low infrared emissivity of ~5 % (3–12 μm), with film hardness exceeding 30 GPa. The diverse functional properties of TMNs and TMBs result from the unique electronic structures, characterized by strong covalent bonds, ionic bonds and metallic bonds [13]. However, these films still possess the drawback of high visible reflectivity. Consequently, devising a simple strategy to reduce the visible reflectivity has emerged as a critical step toward the development of an ultra-high temperature ceramic-based IR-vis compatible stealth film.

Transition metal carbides (TMCs) also exhibit covalent and ionic bonding, along with high electron density [26]. Notably, TMCs generally have higher melting points and hardness as well as excellent oxidation and ablation resistance, suitable for applications in harsher environments. As a typical TMC, HfC, has ultra-high melting point (3900 °C) [27], stable phase structure [28], and high hardness [29]. Most researches currently focus on enhancing the tribo-mechanical properties of magnetron sputtering deposited HfC_x films via controlling the C stoichiometry. For example, Li et al. [30] deposited hard HfC films with different C stoichiometry by reactive magnetron sputtering and gained the maximum hardness of 27.9 GPa at the 56.9 at.% carbon content. Wang et al. [31] achieved a nanocomposite film consisting of HfC_x nanocrystalline and amorphous carbon (a-C) phase at the 76 at.% carbon content, showing great combination of lowest coefficient of friction of 0.1 and lowest wear rate of 1.10×10^{-6} $mm^3/N{\cdot}m$. To our knowledge, there is limited research on the optical properties of HfC_x films.

In the present study, we demonstrate a synergistic strategy that combines adjusting C stoichiometry and energy input to construct a $HfC_{0.91}$ film featuring a low C vacancy contents and high-roughness surface nanostructure to achieve low visible reflectivity while maintaining intrinsically low emissivity in the infrared bands, in addition to the excellent tribo-mechanical performance. Our findings provide a new strategy for the design and preparation of ultra-high temperature ceramic-based IR-vis compatible stealth films.

2. Experiment method

2.1. Sample preparation

HfC_x films were prepared using pulsed DC magnetron co-sputtering system, where Hf (purity 99.95 %) and graphite (purity 99.99 %) targets were sputtered in pure Ar atmospheres (purity 99.99 %). N-type single-crystalline Si platelets ((100) oriented) with a resistivity of ~0.5 Ω m, and copper foils (thickness of 0.05 mm) were used as substrates. To remove the surface impurity, all the substrates were cleaned ultrasonically with acetone, alcohol and distilled water for 20 min, respectively. Prior to deposition, the base pressure of deposition chamber was pumped to 4×10^{-4} Pa by turbomolecular pump and the substrates were heated to 500 °C. A pre-sputtering step using Ar^+ for 10 min was conducted to remove surface oxide layers from the targets. Afterwards, in discharging Ar gas, HfC_x films were deposited at constant work pressure of 0.8 Pa with a float voltage. During the deposition process, the flow rates of Ar was accurately controlled at 40 sccm and the rotating rate of substrate holder was kept at 10 rpm. Four HfC_x films were obtained by varying the applied current on the Hf targets, as listed in Table 1. By adjusting the deposition time, the thickness of films was controlled within the range of 1–2 μm. The Hf and graphite targets were powered using plus power supply (Advanced Energy Pinnacle) operated in middle frequency pulses condition. The pulsed parameter of the two targets were set at 100 kHz and 4 μs.

Table 1
The experimental parameters, C-to-Hf ratio x measured by XPS and WDS, deposition rate, as well as residual stress of the HfC_x films.

Specimen	Current of Hf target (A)	Current of graphite target (A)	Deposition rate (nm/min)	C-to-Hf ratio x	Residual stress (GPa)
H6	0.6	0.5	22.0	0.51	−1.6 ± 0.08
H5	0.5	0.5	16.2	0.63	−1.5 ± 0.11
H4	0.4	0.5	12.1	0.71	−1.9 ± 0.22
H3	0.3	0.5	8.4	0.91	0.5 ± 0.12

2.2. Structure characterization

The phase structure of the deposited films was characterized by X-ray diffraction (XRD, D8-Discover) using Cu Kα ($\lambda = 1.541$ Å) radiation and parameters are set as follows: scan speed of 4°/min, scan range from 20° to 80°, voltage of 40 kV, current of 35 mA. The surface and cross-section morphology of the films were observed using a field emission scanning electron microscope (SEM, Nova Nano SEM450). The chemical composition and states of the elements in films were investigated by X-ray photoelectron spectroscopy (XPS, Thermo Scientific K-Alpha) using Al Kα as X-ray source, and the data were calibrated with the binding energy of C1s (284.8 eV). Prior to the XPS analysis, the sample surface was sputter cleaned for 3 min with 3 keV Ar^+ ions to remove the surface contamination and to avoid the effects of sputtering damages on the surface. Moreover, Electron Probe Micro Analysis (EPMA, JEOL JXA-8230) was also used for elemental analyses of films by wavelength dispersive spectroscopy (WDS). Raman scattering spectroscopy (HORIBA Scientific) with a 532 nm Ar^+ laser and a backscattering optical configuration was used to analyze the structure and defect evolution of films. The nanostructure of films was further investigated via transmission electron microscopy (TEM, Talos F200X) in detail. The H6, H5 and H4 films deposited on the Cu foils were separated from their substrates by chemically dissolving the foils in a diluted $FeCl_3$ solution. The resulting free-standing film flakes were then cleaned and ground into fine powders for TEM investigation. The plan-view TEM specimen of H3 film was prepared by focused-ion beam (FIB, FEI Helios Nanolab 600). The surface roughness was measured by atomic force microscope (AFM, Dimension Icon) with scanning area of 1.0 μm × 1.0 μm.

2.3. Optical and mechanical properties

The reflectance in the range of 200–2000 nm was obtained by a Cary 5000 ultraviolet–visible–near-infrared (UV–vis–NIR) spectrometer. The IR reflectance measurement was performed using a FTIR spectrometer (Thermo Scientific Nicolet iS50R) over a spectral range of 2.5–14 μm. The hardness and Young's modulus were measured using a Nano Indenter G200 system in continuous stiffness measurements (CSM) mode indented by a diamond Berkovitch tip to a maximum depth of 1000 nm. The tribological properties were investigated by UMT-2 ball-on-disc tribometer at room temperature with Al_2O_3 (Diameter = 6 mm) balls sliding counterpart in circles with radius of 1 mm under 1 N load at constant velocity (480 r/min). Wear rates were determined by a volume loss method, where the volume loss was obtained using a 3D optical

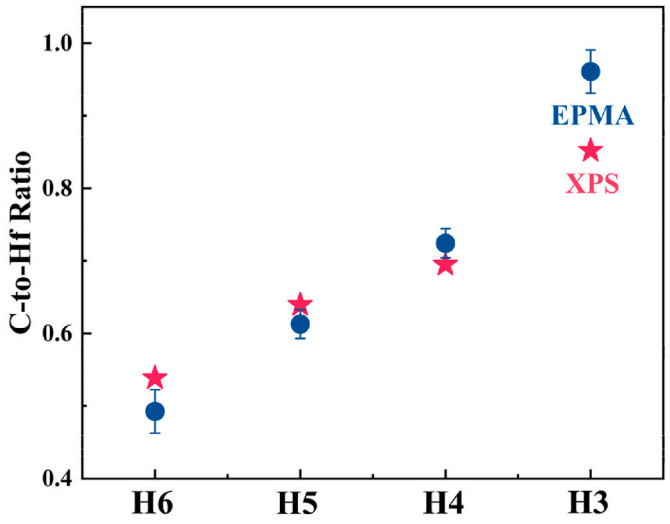

Fig. 1. The C-to-Hf ratio x in the four deposited HfC_x films.

microscope. The intrinsic stress (σ_f) distributed in films has been calculated according to the Stoney equation [31]:

$$\sigma_f = \frac{E_s}{6(1-\nu_s)}\frac{t_s^2}{t_f}\left(\frac{1}{R}-\frac{1}{R_b}\right)$$

Where E_s, ν_s, t_s represent Young's modulus, Poisson's ratio and thickness of the Si (100) substrate, respectively, while t_f and R stand for the thickness and radius curvature for the film, and the calculation results were listed in Table 1.

2.4. Computational methods

All the density functional theory (DFT) calculations were conducted based on the Cambridge Sequential Total Energy Package (CASTEP) module implemented in Materials Studio [32]. The exchange and correction of atomic interactions were treated by the generalized gradient approximation (GGA) method with Perdew-Burke-Ernzerh (PBE) function [33]. The ultrasoft pseudo-potential method [34] is adopted to describe the interactions between valence electrons and ionic cores. A plane-wave basis set is assigned with a cutoff energy of 600 eV. The Brillouin zone is sampled by a Monkhorst-Pack grid [35]. The convergence tolerances of energy, force and displacement for the structure optimization are 5.0×10^{-6} eV/atom, 0.01 eV/Å and 5.0×10^{-4} Å respectively and the self-consistence field (SCF) is set as 1.0×10^{-6} eV/atom.

A supercell HfC model with the rock-salt (B1) structure containing 64 atoms is firstly built based on a conventional 8-atomic cell. A series of defective HfC_x (x = C/Hf, atomic ratio) models with the introduction of various concentrations of Hf and C vacancies are further built based on the special quasi-random structure (SQS) method [36] which are generated by using the Alloy Theoretic Automated Toolkit (ATAT) [37]. The k point for all the models is set as ($3 \times 3 \times 3$) for structure optimization and ($6 \times 6 \times 6$) for DOS calculation.

3. Results and discussion

3.1. Microstructure analysis of the HfC_x film

Fig. 1 shows the measured C-to-Hf ratio x in the four deposited HfC_x films. It includes the results from both XPS and WDS analysis, plotted as red pentagram and blue circles, respectively. The results for H6, H5 and H4 films exhibit the good agreement between the two independent measurement methods. The discrepancy in values for H3 film, which contains high levels of C, may be attributed to preferential sputtering during surface cleaning for XPS measurements and/or the experimental uncertainties for light element determination using WDS analysis [38]. Thus, the average values from these two methods are considered as the C stoichiometry of the HfC_x films, as listed in Table 1. The plotted C-to-Hf ratio increases from $x = 0.51$ to 0.63, 0.71 to 0.91 with decreasing the current of Hf target.

Fig. 2 shows the surface and cross-section morphology of H6-H3 films analyzed by SEM. The H6 and H5 films exhibit a uniform compact surface with a typical columnar structure in the cross section. For H4 and H3 films, the surface become rougher, accompanied by a more pronounced columnar structure. According to the empirical structure zone model [39], the columnar morphology of sputtered films

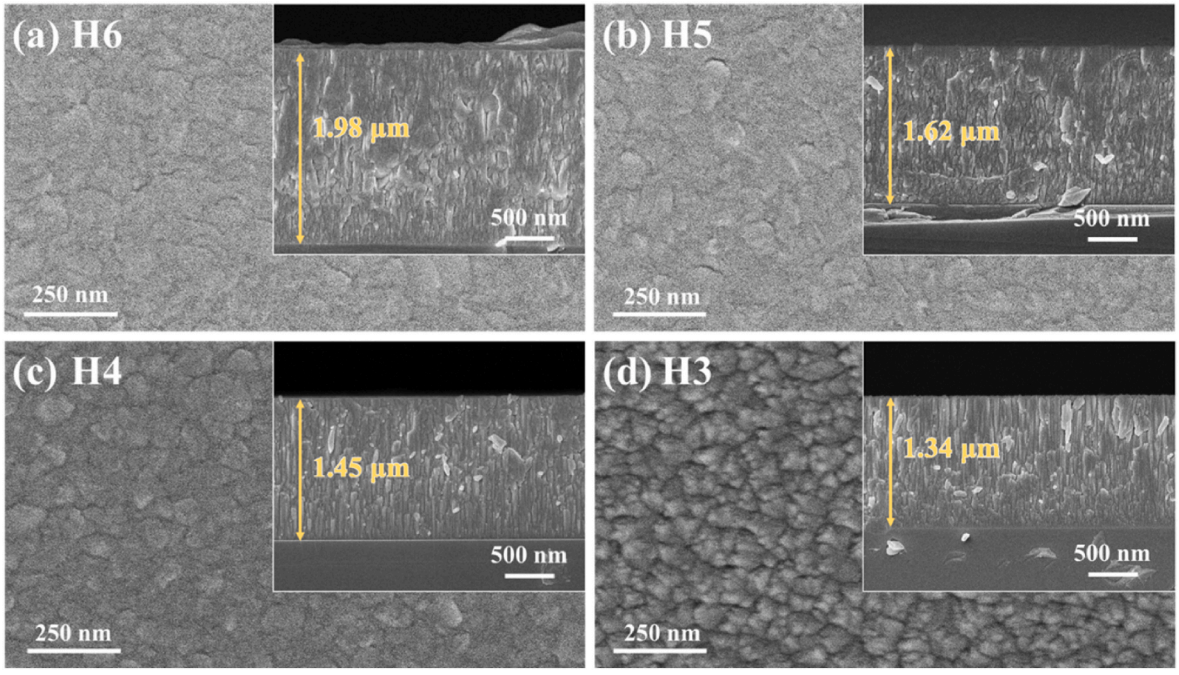

Fig. 2. Surface and cross-section morphology of HfC_x films.

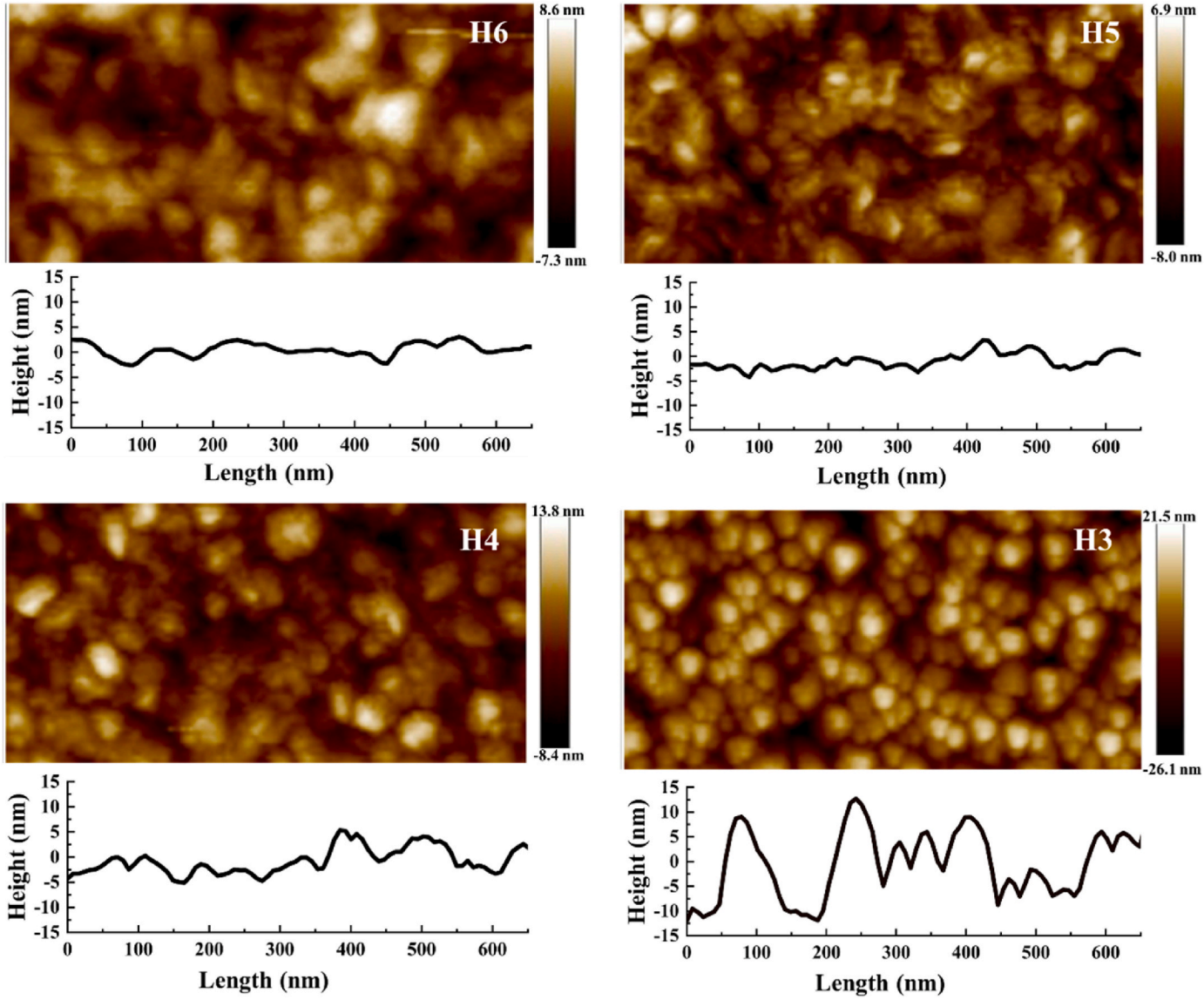

Fig. 3. 2D-AFM images and corresponding 1-D outline of HfC_x films.

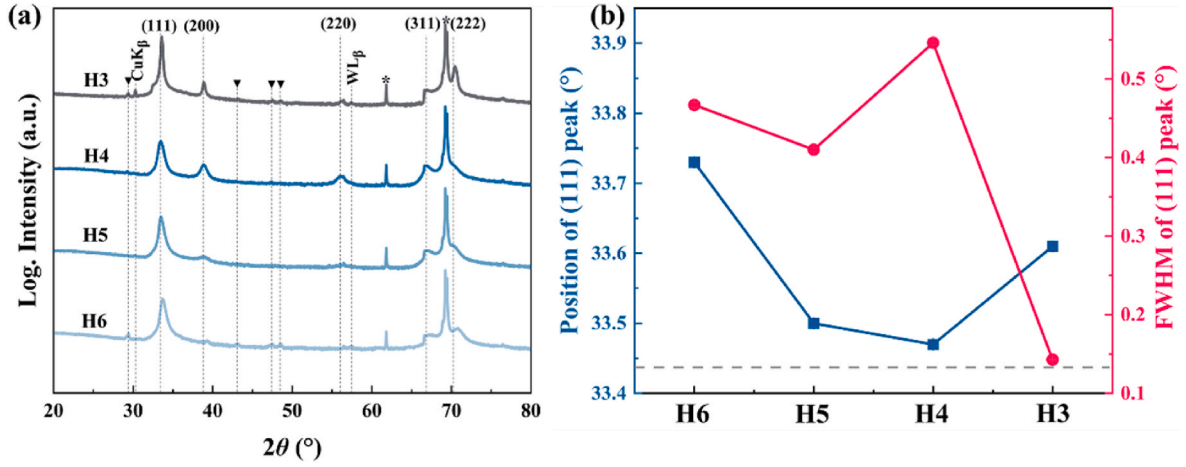

Fig. 4. (a) X-ray diffraction (XRD) patterns of HfC_x films. The vertical gray dotted line denotes the standard diffraction peaks of HfC phase with rock salt structure, * represents the single-crystalline Si substrate (100 oriented) peaks and ▼ represents the diffraction peaks of Hf-Si phase. (b) A detailed peak profile analysis with respect to the position and FWHM of (111) peak.

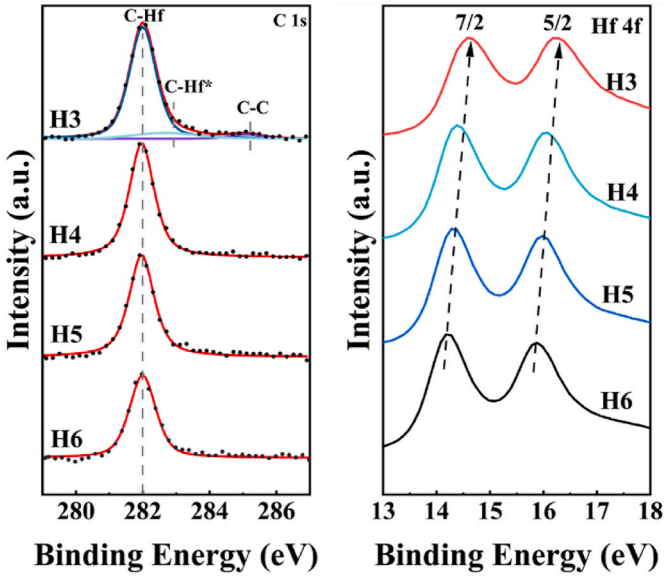

Fig. 5. High-resolution XPS spectra of the C 1*s* and Hf 4*f* peaks from HfC_x films.

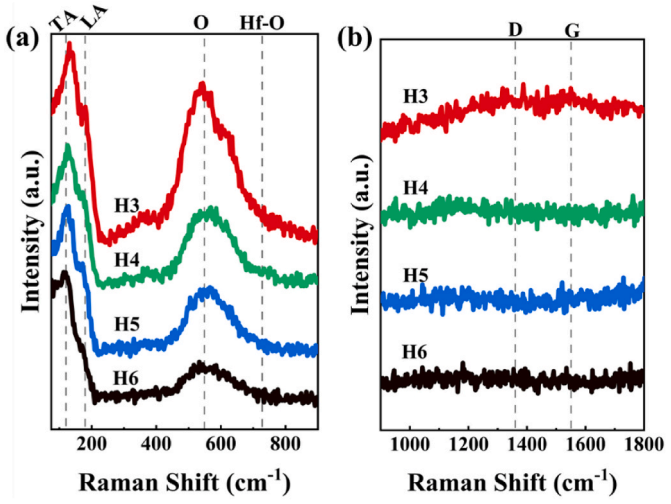

Fig. 6. HfC_x films Raman spectroscopy for (a) low Raman shift (75 and 900 cm^{-1}) and (b) high Raman shift (900 and 1800 cm^{-1}).

was a consequence of slow adatom mobilities [40]. So, the morphology transition of HfC_x may be contributed to two main factors: (i) the decreased energy input, resulting from a reduced Hf target current, leads to low adatom mobilities; (ii) the homologous temperature (T_s/T_m, where T_s is the growth temperature of 773 K and T_m is the melting point of HfC_x in K) decreases with increasing C stoichiometry of HfC_x films, thereby further reducing the adatom mobilities. Slow adatom mobilities promote kinetic roughening [41], as the tops of the protruding grains capture sputtered atoms at higher rates. As a result, the columnar structure in HfC_x films is enhanced as the Hf target current decreases.

A clearer perspective of the surface morphology is provided by the 2D-AFM images, accompanied by the corresponding 1-D outline (Fig. 3). Consistent with the SEM results, with the decrease of Hf target current, the surface of the film become rougher. The variation in surface roughness is quantified by the root mean square (R_q), yielding the following results: H6 is 2.4 nm, H5 is 2.2 nm, H4 is 3.2 nm, and H3 is 6.9 nm. It is to be noted that the H3 film exhibits a significantly larger surface roughness, characterized by abundant pits and bumps with ~20 nm and spacings of hundreds of nanometers.

Fig. 4a shows out of plane X-ray diffraction scans for H6-H3 films deposited on Si (100). The H6 and H5 films exhibit C-deficient fcc rock salt HfC phase (ICDD PDF 65–0975) with strong (111) preferred orientation and broad diffraction peaks. The diffraction profile from H4 and H3 films, which contain more C, clearly include both (200) and (220) out-of-plane orientations of HfC phase, indicating the rock salt carbide reverts to polycrystalline texture. This transition is also associated with the adatoms mobilities. When the mobility of Hf adatoms is high, the (111) grains expand at the expense of other indexed grains, resulting in the development of a (111)-preferred orientation. This occurs because the diffusivities and potential energies of Hf adatoms are lower on 111-oriented grains compared to others, leading to a higher chance of Hf adatoms being captured by the 111 grains [41]. As the Hf target current decreases, the reduced kinetic energy of Hf sputtered atoms or ions slows the adatoms mobility on grain growth surfaces, thereby increasing the probability of their capture by all indexed planes rather than tending to being captured by the 111-oriented grains, which promotes the formation of a polycrystalline texture. Additionally, several peaks marked with "▼" are associated with the Hf-Si phase, which may arise from a solid-state reaction between the film and the Si substrate [42]. A detailed peak profile analysis with respect to the position and FWHM of (111) peak is presented in Fig. 4b. The position of (111) for the stoichiometric stress-free HfC is indicated by dotted lines according to data from ICDD PDF 65–0975. Notably, although the H6, H5, and H4 films exhibit in-plane compressive stress (see Table 1), their (111) peak position remain higher than that of stoichiometric stress-free HfC. This observation indicates that these films are sub-stoichiometric HfC_x materials, characterized by a significant presence of carbon vacancies. The (111) peak position initially shifts towards lower angles until x reaches 0.71 (H4 film), likely due to an increased occupancy of carbon at the HfC sublattice sites, resulting in lattice expansion. Conversely, the (111) peak position of H3 shifts towards higher angles, which may be attributed to transitions to in-plane tensile stress. Furthermore, the evolution of FWHM could be ascribed to the synergistic effects of grain refinement and the lattice distortion degree in the films.

To further identify the chemical bonding state, XPS analysis was performed for the HfC_x films. Fig. 5 shows the high-resolution XPS spectra of the C 1s and Hf 4f peaks and the related fitting components for HfC_x films. All the spectra were calibrated by C 1s with a binding energy of 284.6 eV. The H6, H5 and H4 films show a single C 1s peak at ~282 eV, representing the C-Hf bonds, with intensity increasing in correlation with C stoichiometry. The XPS spectrum from the H3 film can be fitted with three curves representing C-Hf, C-Hf*, and C-C peaks, respectively. The C-Hf peak is associated with C in bulk HfC, while the C-Hf* peak pertains to C near the HfC surface, where the reduced number of Hf neighbors leads to a decrease in charge transfer, resulting in increased binding energy [31,38]. The C-C peak located at ~285 eV potentially indicates a saturated carbide lattice with an excessive C second phase [38]. The amount of bonded C also affects the relative peak positions of Hf, as shown by the Hf 4f7/2 and Hf 4f5/2 peaks. The Hf binding energy gradually increases with C stoichiometry indicating an increasing concentration of C-Hf bonds.

Fig. 6 shows Raman spectra of HfC_x films. As shown in Fig. 6a, the occurrence of first-order acoustic (TA, LA) and optical peaks (O) at approximately 120, 180 and 555 cm^{-1} indicate that HfC_x films with varying C stoichiometry consistently maintain a NaCl crystal structure, which is corroborated by XRD results. The intensity and frequency of the first-order acoustic branch are derived from the vibration amplitude and valence electron concentration of the metal ion (Hf^{+} in this study) in the crystal lattice, respectively [43]. The O peak arises from the characteristic of C atoms. The increase in O peak intensity with C stoichiometry is attributed to the lower C vacancy level, which leads to the enhanced vibration intensity of total C atoms [44]. A similar phenomenon is reported in Ref. [45], where the relative intensity of the O peak to A peak (I_O/I_A) increases as x increases in HfN_x films. Additionally, a small peak is observed near to 700-750 cm^{-1}, attributed to the oxygen in the lattice. The ubiquitous oxygen may come from residual oxygen in the chamber

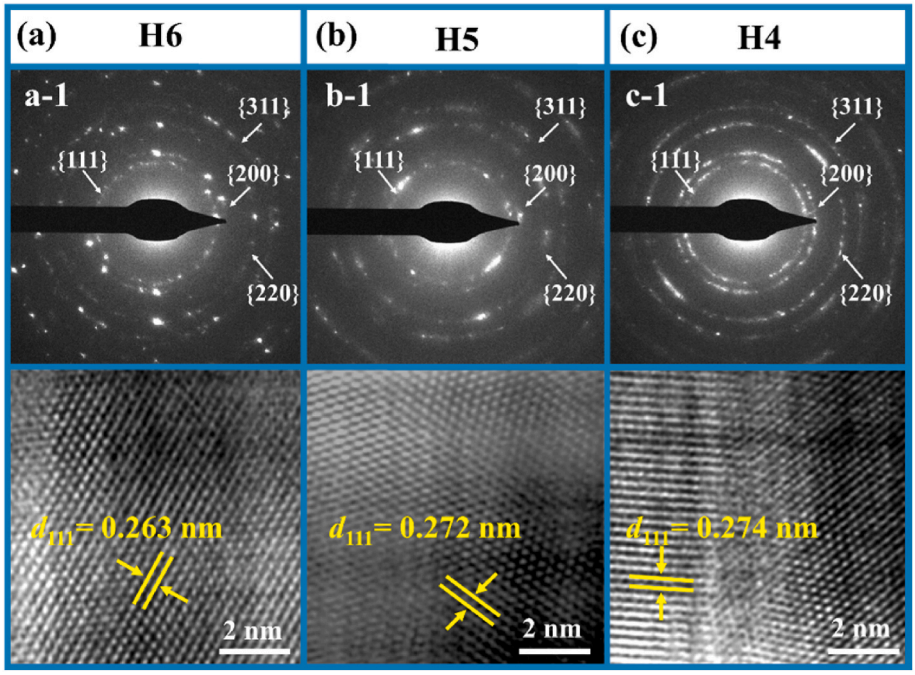

Fig. 7. Selected area electron diffraction (SAED) pattern and high-resolution TEM (HRTEM) images (with d_{111} spacing) of H6 (a), H5 (b) and H4 (c) films.

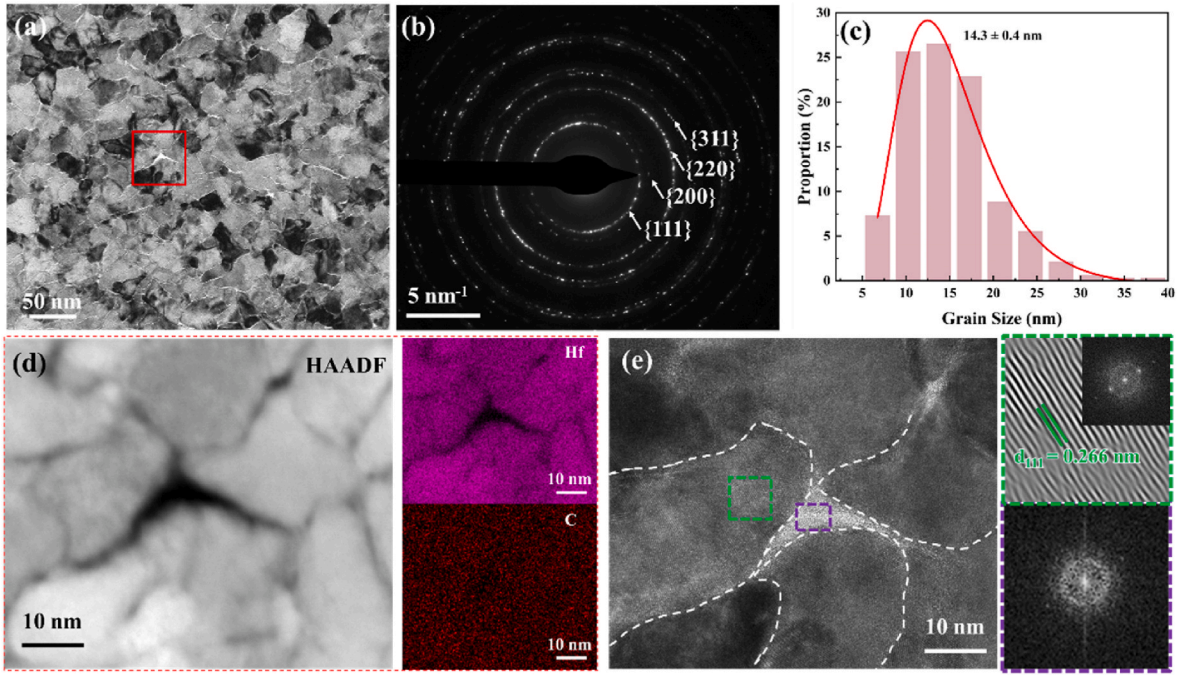

Fig. 8. Typical TEM images of structural overview of the H3 film: (a) TEM image of the plan-view; (b) SAED image of plan-view; (c) Statistical data analysis of grain size from TEM images of the plan-view; HAADF image with element mapping of Hf and C (d) and HRTEM image analyses (e) corresponding to red square in (a). (For interpretation of the references to color in this figure legend, the reader is referred to the Web version of this article.)

atmosphere, as well as natural surface oxidation that uncontrollably occurs on metals in contact with moisture in the environment. As shown in Fig. 6b, only H3 film exhibits D-peak (around 1340 cm^{-1}) and G-peak (near 1590 cm^{-1}) of the amorphous carbon (a-C) phase [46], further indicating the C-C bond observed in XPS belongs to a-C phase.

In order to gain insight into microstructure evolution in HfC_x films, we further conducted the TEM characterization on the HfC_x films. Fig. 7 shows the selected area electron diffraction (SAED) pattern and the corresponding high-resolution TEM (HRTEM) for H6, H5 and H4 films. The SAED patterns of the three films only show clear spots and rings correlated with fcc structure with {111}, {200}, {220} and {311} planes of HfC, indicating a typical polycrystalline structure with high crystallinity. In addition, the HRTEM images of the films all reveal well-defined lattice fringes with measured interplanar spacing (d_{111}) of 0.263, 0.272 and 0.274 nm for H6, H5 and H4 films, respectively.

The plan-view TEM image of the H3 film, presented in Fig. 8a, reveals a nanograin structure with varying orientations. The corresponding SAED pattern, shown in Fig. 8b, exhibits only spots and rings

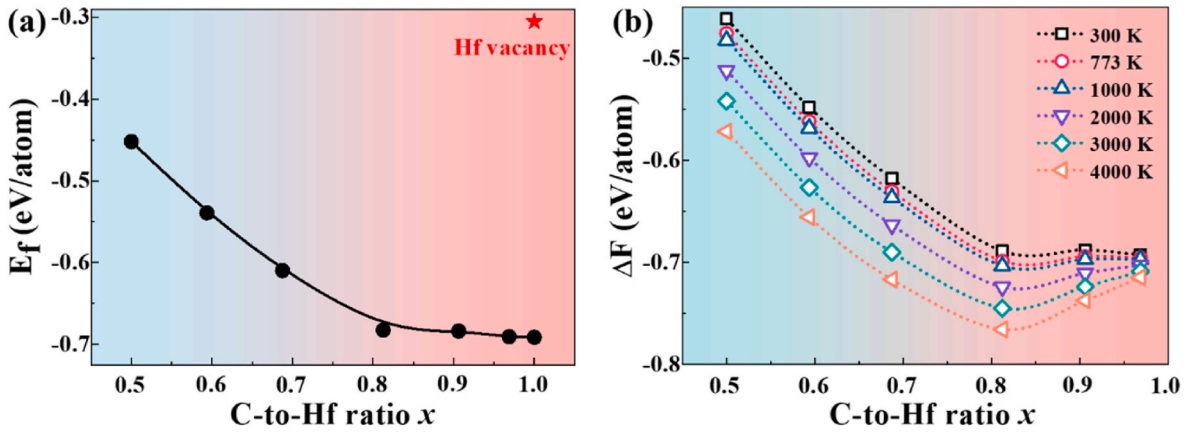

Fig. 9. (a) Formation energy and (b) Helmholtz free energy of HfC_x films with varying C-to-Hf ratio x.

associated with the HfC phase. Statistical analysis of more than 5 plan-view TEM images indicates that the average grain size is approximately 14.3 ± 0.4 nm (Fig. 8c). After careful observation, bright regions can be identified between the HfC nanograins and at the triple junctions. To further elucidate the composition and structure of these bright regions, the region marked by the red box in Fig. 8a is analyzed by high-angle annular dark-field scanning transmission electron microscopy (HAADF-STEM) (Fig. 8d) and HRTEM (Fig. 8e). As illustrated in Fig. 8d, HAADF-STEM and the corresponding EDS mapping analysis reveal that Hf is concentrated within the grains. Notably, C is distributed relatively evenly across the grains and at the triple junctions. This observation suggests that the atomic density at the triple junctions is lower than that within the grains. Furthermore, HRTEM analysis (Fig. 8e) further elucidates the amorphous nature of the triple junctions. Combined with the analysis results from XPS and Raman, a reasonable explanation can be formulated as follows: the reduction in adatom mobility, caused by the

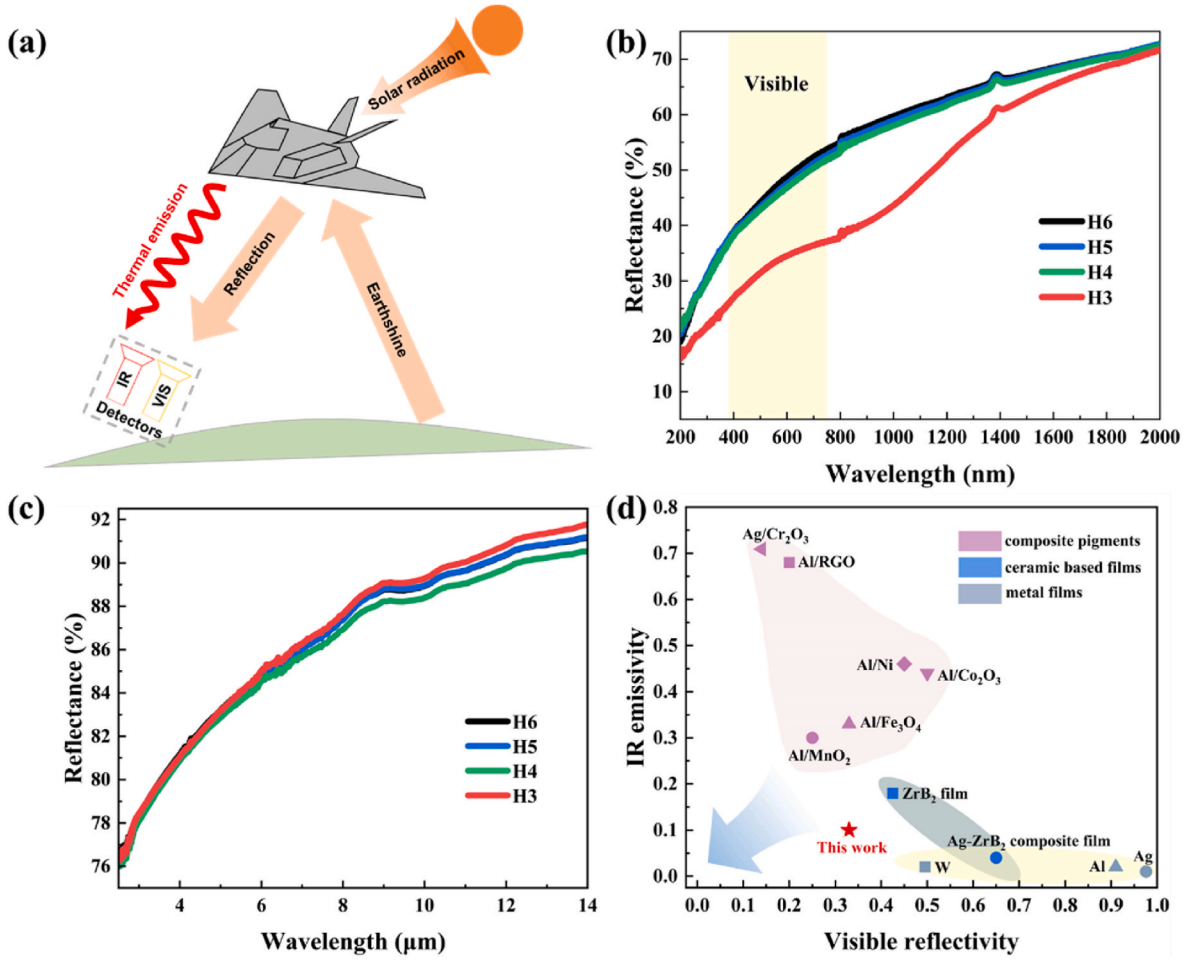

Fig. 10. (a) Two primary signal sources: the reflection of solar radiation and earthshine, as well as thermal emission of the object. (b) Reflectance spectra of HfC_x films in the wavelength range of 200–2000 nm. (c) Reflectance spectra of HfC_x films in the wavelength range of 2.5–14 μm. (d) Comparison of the visible reflectivity and IR emissivity of various camouflage materials, including composite pigments [48–53], ceramic based films [15,25], metal films [6], and this work.

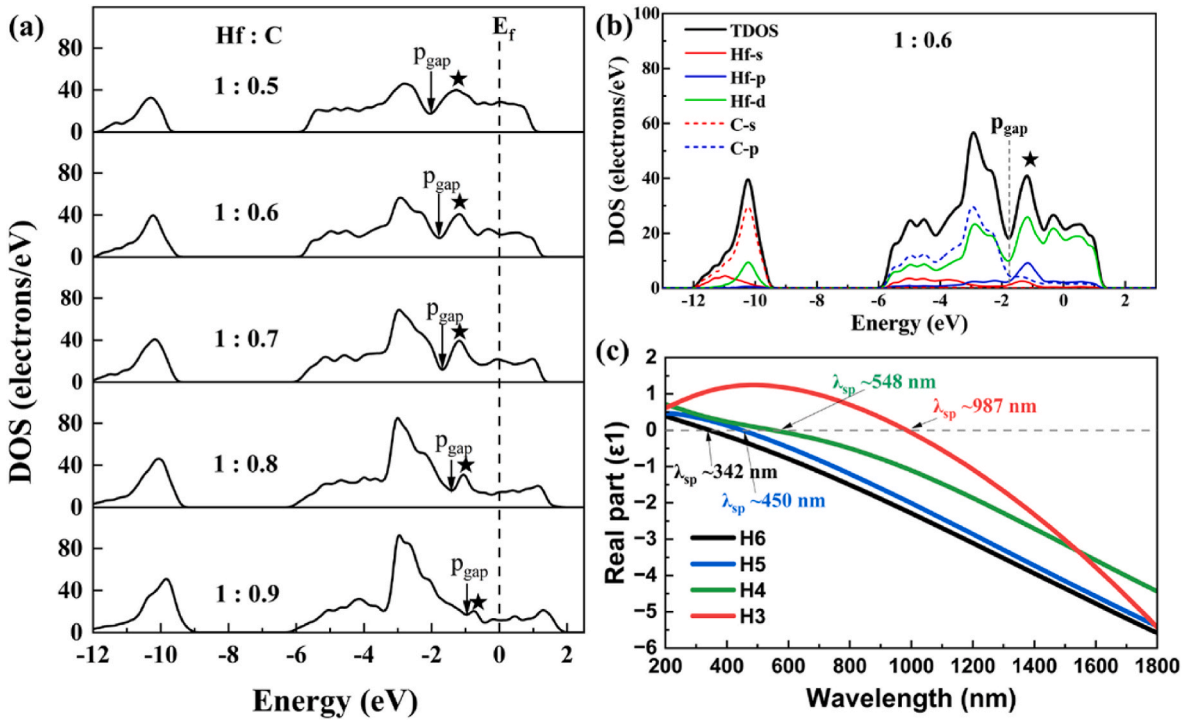

Fig. 11. (a) The total density of states of HfC_x films with different C stoichiometry; (b) electronic structure of carbide with Hf: C = 1 : 0.6 showing C-s, C-p, Hf-s, Hf-p, Hf-d contribution; (c) the real parts of dielectric function of HfC_x films.

decrease in the Hf target, enhances the atomic shadowing effect; this effect obstructs deposition in the valleys between columnar grains, resulting in an under-dense structure; the a-C phase is more likely to nucleate and grow in the voids of triple junctions. Additionally, the interplanar spacing of the (111) plane of H3 film is measured as 0.266 nm, showing the order: H6 < H3 < H5 < H4. The trend is consistent with XRD analysis (Fig. 4).

It is noteworthy that the H6 film (x = 0.51), which has a 49 % C vacancy, still exhibits a single fcc carbide phase. In contrast, the H3 film (x = 0.91), with 9 % C vacancy, contains an a-C phase. In order to evaluate the phase stability of HfC_x films from a chemical perspective, the formation energy (E_f) and Helmholtz free energy (ΔF) of Hf-C systems with different stoichiometries are calculated using the following formulas [47].

$$\Delta F = E_f - T \cdot S^C \tag{1}$$

$$E_f = E^{per/def} - \frac{1}{\sum_i n_i} \sum_i n_i . E_i \tag{2}$$

$$S^C = \frac{1}{2} \cdot k_B \cdot (x \cdot \ln(x) + (1-x) \cdot \ln(1-x)) \tag{3}$$

where $E^{per/def}$ is the total energy per atom of the perfect (per) or defected (def) structure, E_i is the total energy per atom of the species i in its stable bulk structure and n_i is the number of atoms of species i in the supercell, wherein I = Hf, C, S^C is the configurational entropy related to the C vacancy, k_B is the Boltzmann constant. T is temperature.

As shown in Fig. 9a, the formation energy E_f decreases from −0.45 eV to −0.7 eV with increasing x from 0.5 to 1.0, but significantly increases to −0.3 eV when introducing 5 % vacancy at the Hf sublattice as indicated by red pentagram. This suggests that the formation of vacancies at the C sublattice is significantly less expensive than at the Hf sublattice. Fig. 9b illustrates that the Helmholtz free energies (ΔF) of HfC_x with x = 0.5–1.0 are all negative, suggesting that samples with corresponding C vacancies can be synthesized in practical experiments. Moreover, HfC_x exhibits the lowest ΔF when x = 0.81, i.e., the highest chemical stability, indicating that excess C tends to precipitate in the form C-C bonds when x above 0.81. Consequently, the H6 film with 49 % C vacancy can maintain a single carbide structure, while the H3 film with 9 % C vacancy shows the presence of an a-C phase in this experiment.

3.2. Optical properties of the HfC_x film

As shown in Fig. 10a, objects typically betray their presence through two types of signals: 1) reflected signals from external light sources, such as solar radiation and earth shine; and 2) thermal emission signals originating from the objects themselves. Consequently, low visible reflectivity and low infrared emissivity (high reflectivity) are essential for IR-vis compatible stealth films. Figs. 10b and c illustrate the reflectance spectra of HfC_x films across the wavelength ranges of 200–2000 nm and 2.5–14 μm, respectively. These ranges encompass the typical visible (380–780 nm) and infrared detection bands (3–5 μm and 8–14 μm). The sequence of visible reflectance for the four films is as follows: H6 > H5 > H4 > H3. These films exhibit very similar reflectance within the 3–5 μm wavelength range, while the sequence of reflectance across the 8–14 μm wavelength range is: H3 > H6 ≈ H5 > H4. It can be found that the H3 film exhibits the best IR-vis compatible stealth performance. Most importantly, as shown in Fig. 10d, this combination of visible reflectivity and IR emissivity of H3 film is superior to that of most reported IR-vis compatible stealth materials. Consequently, we successfully developed a monolayer $HfC_{0.91}$ film that has great potential for actual multispectral camouflage with low visibility and low thermal emission.

To explore the origin of the reflectivity evolution of HfC_x, first-principles calculations were performed to investigate the effect of C stoichiometry on the electronic structure. Fig. 11a shows the total density of states for 10, 20, 30, 40, and 50 % vacant C sites. The minima in the electronic structure represents the pseudogap (p_{gap}). Energy states below the p_{gap} are bonding in nature whereas states above p_{gap} exhibit antibonding characteristics [46]. To identify the constituents that contribute bonding and antibonding electrons, a partial density of states

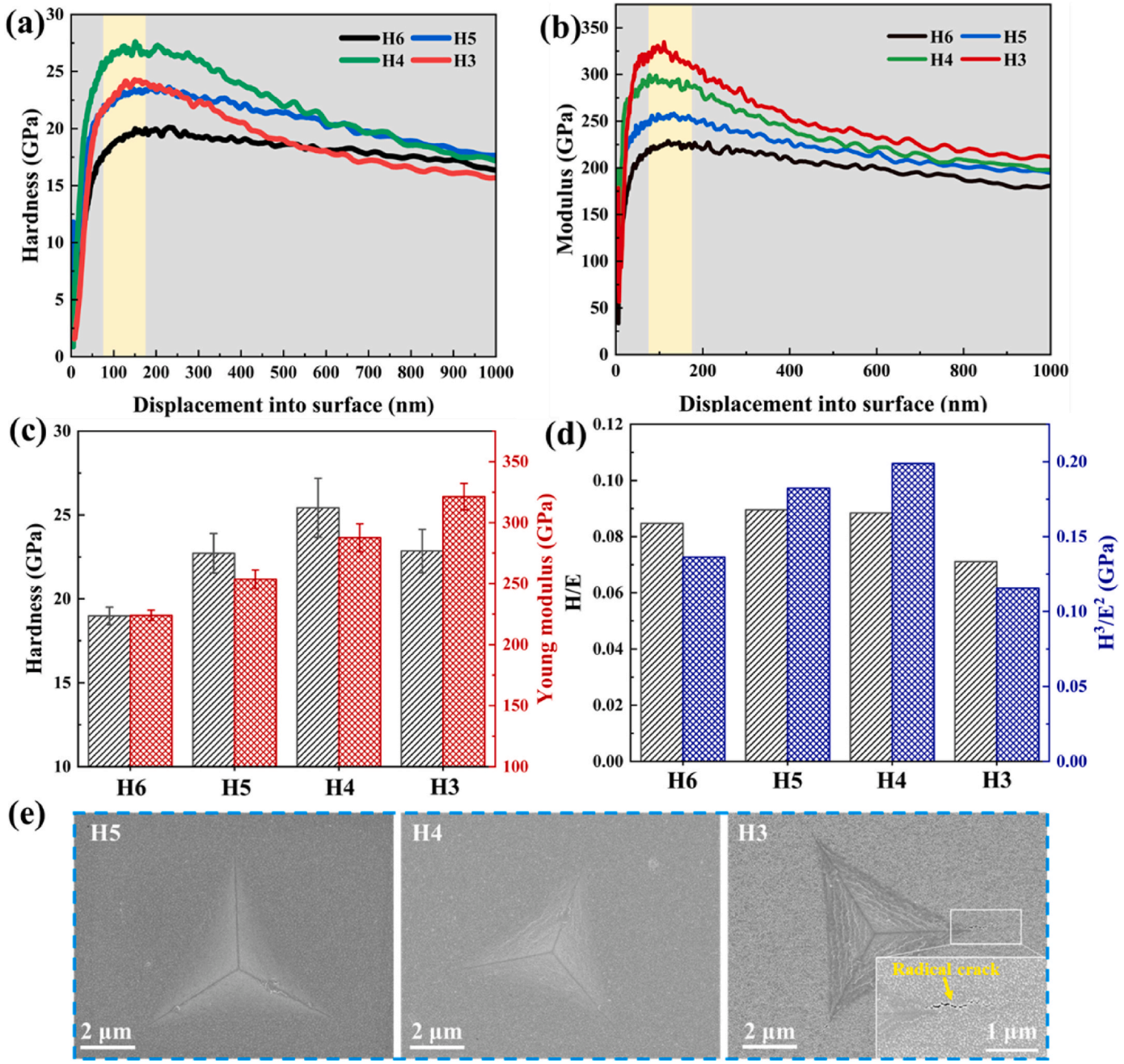

Fig. R12. (a) *H*-displacement curves, (b) *E*-displacement curves, (c) *H* and *E*, and (d) the calculated *H/E* and H^3/E^2 of HfC_x films; (e) SEM micrographs of indent imprints for H5, H4 and H3 films.

(pDOS) analysis for 40 % vacant C sites was completed. As shown in Fig. 11b, the C-p orbital and Hf-d orbitals contribute strongly to the energy states below the p_{gap}, with a peak at −3 eV, while the majority of antibonding states are associated with Hf-d orbitals which can contribute free electrons [13]. As C stoichiometry decreases, a shift in the p_{gap} to lower energy levels is observed, accompanied by an increasing population of antibonding states above it, suggesting an enhancement in the concentration of free electrons. They have an important contribution from the free electrons to the plasma energy which is closely consisted with reflectivity [13,15]. To obtain plasma energy of films, the real parts ($\varepsilon 1$) of dielectric permittivity were calculated based on the refractive index (n) and extinction coefficient (k), given by [54].

$$\varepsilon 1 = n^2 - k^2 \quad (4)$$

The $\varepsilon 1$ of dielectric function of HfC_x films are shown in Fig. 11c. The $\varepsilon 1$ of HfC_x films demonstrate a transition from positive to negative values as a function of wavelength, indicating the existence of local-surface-plasmonic-resonance (LSPR) [55]. The crossover plasma energy, $E_{sp} = hc/\lambda_{sp}$, where h is Plancks constant, c is the speed of light, and λ_{sp} is wavelength, can be calculated at $\varepsilon 1 = 0$, known as the epsilon-near-zero (ENZ) point [56]. It can be found that the λ_{sp} of HfC_x films exhibits a red shift with increasing C stoichiometry, corresponding plasma energy decreases from 3.55 to 1.25 eV. According to Drude's classical theory, the increase in plasma energy results in the increase in the reflectivity [13,15], and the sequence of the four films should be: H6 > H5 > H4 > H3. However, the measured infrared reflectance does not match the trend predicted by the Drude's classical theory. The H3 film containing the most C content exhibits the highest reflectivity across the 8–14 μm wavelength range. This may be due to the fact that HfC are

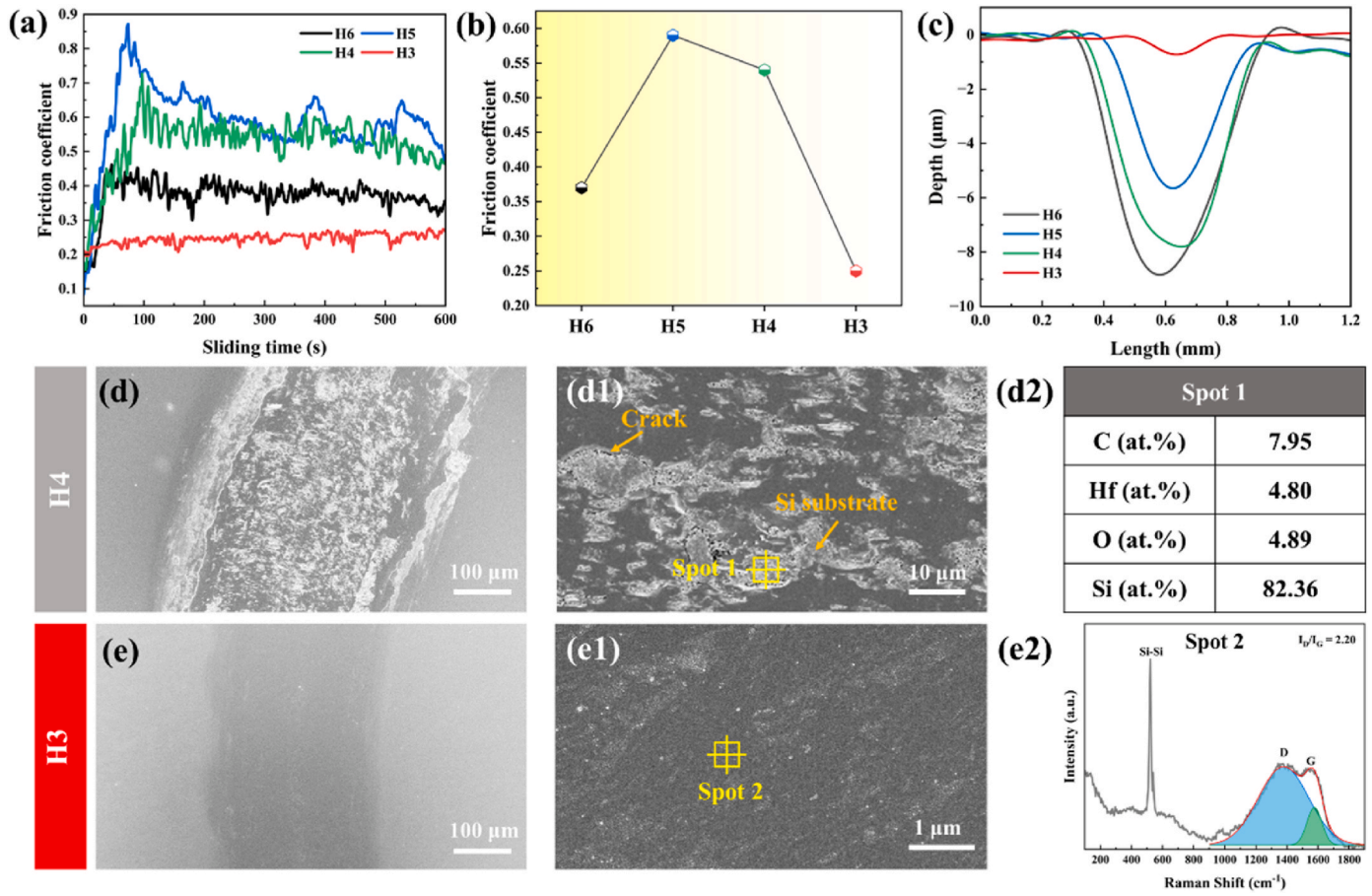

Fig. 13. (a) The friction coefficient curves, (b) friction coefficient and (c) wear curves for HfC_x films. (d, d1, d2) SEM-EDS analyses of the worn tracks of H4 film. (e, e1, e2) SEM and Raman analyses of worn tracks of H3 film.

composed of a combination of covalent, ionic, and metallic bonds, rather than pure metal bonds. Therefore, lattice vibration absorption is another important factor affecting infrared emissivity [5]. The stronger the bond energy, the more difficult the molecular vibrations are, thus the lower the emissivity (the higher reflectivity) will be. With the increase in C stoichiometry, the content of covalent bonds rises, leading to enhanced bond energy. This improvement results in increased infrared reflectivity of HfC_x film, which is why H3 film exhibits the highest reflectivity. Furthermore, it is important to note that although the H3 film shows the lowest visible reflectivity, as anticipated by theory, its reflectivity decreases significantly compared to the other films which experience only slight changes. This may be attributed to its surface nanostructure with significantly larger roughness, which contributes to enhanced multiple scattering absorption [24,57]; notably, this roughness is still too small in scale to result in strong interaction with long-wavelength infrared light [58].

3.3. Tribo-mechanical properties of the HfC_x films

The hardness (H) and Young's modulus (E) of the HfC_x films were measured using nanoindentation in continuous stiffness mode, with the H-displacement and E-displacement curves presented in Fig. 12a and b, respectively. With the increase of displacement into surface, the H and E values exhibit an initial increase to a maximum value followed by a subsequent decrease, and thus H and E values were determined by taking the average values within the penetration depth of 75–175 nm to minimize both substrate roughness and substrate effects, as shown in Fig. 12c. The H value gradually increases from 18.9 ± 0.5 GPa for H6 film to 25.4 ± 1.7 GPa for H4 film, and then decreases to 22.9 ± 1.3 GPa for H3 film. The Young's modulus increases linearly from 223.9 ± 4.2 GPa for H6 film to 321.4 ± 10.8 GPa for H3 film. According to the literatures [59,60], both hardness (H) and elastic modulus (E) are associated with the wear resistance of thin films. High hardness is directly correlated with greater wear resistance; however, a high elastic modulus may induce stress concentrations that diminish the wear resistance of the film. The elastic index can be defined as H/E, and the plasticity indicators like (H^3/E^2) are frequently utilized to assess the wear resistance of the films. The H/E and H^3/E^2 values of films are illustrated in Fig. 12d. The H4 film exhibits the highest values of H/E and H^3/E^2, while the H/E and H^3/E^2 values for H3 film slightly decrease to 0.07 and 0.12, respectively. Furthermore, detailed observations on the indents at the indentation depth of 1000 nm were conducted by SEM as shown in Fig. 12e. The H5 film and the H4 film are both crack-free, exhibiting excellent toughness. In contrast, three distinctly radical cracks are observed around the indent for the H3 film indicating inferior fracture toughness, which may be attributed to the under-dense structure of the H3 film.

Tribological experiments were performed on HfC_x films using ball-on-disc tests. The results of friction coefficient and wear curves are presented in Fig. 13a-c. Clearly, the H3 film exhibits the lowest friction coefficient (~0.24) throughout the wear process and a narrow and smooth wear track, which is profoundly different from the wide and deep wear track of other HfC_x films. Hence, the H3 film has an orders of magnitude reduction in specific wear rate (2.3×10^{-5} mm^3/N·m) compared to the H4 (5.3×10^{-4} mm^3/N·m), H5 (4.4×10^{-4} mm^3/N·m) and H6 (5.7×10^{-4} mm^3/N·m) films. It is well known that films with higher H/E and toughness usually demonstrate better wear-resistance performance. However, despite the H3 film having lower H/E and

toughness compared to the H4 film, it displays superior wear-resistance. In order to find out the reason, SEM-EDS and Raman experiments were carried out on the worn surface of H4 and H3 films, as shown in Fig. 13d and e. The wear track of the H3 film becomes significantly narrower and transitions into a very smooth surface with invisible cracks compared to the H4 film. Furthermore, quantitative EDS analyses of spot 1 indicate that the H4 film is worn out. For the H3 film, the Raman results (Fig. 13e2) from the wear track show an intensified D peak and G peak compared to the film surface (see Fig. 6), signifying a marked increase in graphitic structures. This finding suggests that the introduction of the a-C phase in the H3 films creates a new friction interface characterized by weak shear force [31,61], resulting in a reduced friction coefficient and wear rate. In contrast, no lubricating layer forms at the friction interface when the H6, H5 and H4 films slide against counterparts, resulting in a high friction coefficient and wear rate.

4. Conclusion

In this work, the microstructure evolution, optical properties and tribo-mechanical performance of pulse magnetron co-sputtered HfC_x film were investigated. The key conclusions obtained from this investigation are summarized as follows:

(1) By reducing the Hf target current, the C stoichiometry in HfC_x films increased and the energy input decreased. The resulting $HfC_{0.91}$ film exhibited a mixed phase of rock salt carbide and a-C phase due to the stoichiometry with the highest chemical stability is $HfC_{0.81}$ according to first-principles calculations. The $HfC_{0.91}$ film also exhibited significantly larger surface roughness due to enhanced the kinetic roughening effect.
(2) The $HfC_{0.91}$ film exhibited the low average infrared emissivity in the 8–14 μm range of 0.1 and the low average visible reflectivity of 0.33 due to the synergistic effect of reduced in lattice vibration absorption, reduced plasma energy and enhanced multiple scattering absorption.
(3) The $HfC_{0.91}$ film exhibited enhanced wear-resistance due to a self-lubrication a-C tribo-film formed on the wear tracks during sliding.

Consequently, the $HfC_{0.91}$ film shown the favorable combination of properties of IR-vis compatible stealth and wear-resistance, presenting promising potential for application in actual multispectral camouflage systems designed for harsh environments.

CRediT authorship contribution statement

Gaopeng Zou: Writing – review & editing, Writing – original draft, Methodology, Data curation. **Qianqian Wang:** Writing – review & editing, Methodology, Funding acquisition. **Ruixin Sheng:** Methodology. **Ligang Sun:** Writing – original draft, Visualization, Methodology, Funding acquisition. **Qiyue Shao:** Methodology. **Xuhai Zhang:** Methodology. **Zhe Jia:** Writing – review & editing, Methodology, Formal analysis. **Baolong Shen:** Writing – review & editing, Supervision, Methodology, Funding acquisition, Formal analysis.

Declaration of competing interest

The authors declare that they have no known competing financial interests or personal relationships that could have appeared to influence the work reported in this paper.

Acknowledgements

This work was supported by National Natural Science Foundation of China (52231005), Jiangsu Provincial Key R&D Program (BE2021088), Open Research Fund of Jiangsu Key Laboratory for Advanced Metallic Materials, Southeast University (AMM2023B05), Opening Project of Jiangsu Key Laboratory of Advanced Structural Materials and Application Technology (ASMA202302), Guangdong Basic and Applied Basic Research Foundation (2022A1515011402), Science, Technology and Innovation Commission of Shenzhen Municipality (GXWD20231130102735001, ZDSYS20210616110000001), Development and Reform Commission of Shenzhen (XMHT20220103004).

References

[1] P. Wu, Y. Zeng, J. Wang, Z. Zhao, J. Li, Y. Sun, X. Tang, W. He, Realizing microwave-infrared compatible stealth via single 8YSZ coating, J. Adv. Ceram. (2024), https://doi.org/10.26599/jac.2024.9220954.
[2] Y. Wu, S. Tan, Y. Zhao, L. Liang, M. Zhou, G. Ji, Broadband multispectral compatible absorbers for radar, infrared and visible stealth application, Prog. Mater. Sci. 135 (2023) 101088, https://doi.org/10.1016/j.pmatsci.2023.101088.
[3] L. Jin, Y. Zhao, C. Chen, J. Zhang, Y. He, C. Yin, N. Wu, J. Tang, S. Xing, Application, development, and challenges of stealth materials/structures in next-generation aviation equipment, Appl. Surf. Sci. Adv. 19 (2024) 100575, https://doi.org/10.1016/j.apsadv.2024.100575.
[4] H. Zhu, Q. Li, C. Zheng, Y. Hong, Z. Xu, H. Wang, W. Shen, S. Kaur, P. Ghosh, M. Qiu, High-temperature infrared camouflage with efficient thermal management, Light Sci. Appl. 9 (2020) 60, https://doi.org/10.1038/s41377-020-0300-5.
[5] X. Fan, S. Li, W. Zhang, X. Zhang, J. Mou, Low infrared emissivity of a Ti_3AlC_2 MAX ceramic for high-temperature thermal camouflage, J. Eur. Ceram. Soc. 44 (2024) 5503–5515, https://doi.org/10.1016/j.jeurceramsoc.2024.03.043.
[6] Z. Deng, Y. Su, W. Qin, T. Wang, X. Wang, R. Gong, Nanostructured Ge/ZnS films for multispectral camouflage with low visibility and low thermal emission, ACS Appl. Nano Mater. 5 (2022) 5119–5127, https://doi.org/10.1021/acsanm.2c00088.
[7] J.S. Lim, N. Lee, T. Kim, I. Chang, J. Nam, H.H. Cho, Multiresonant selective emitter with enhanced thermal management for infrared camouflage, ACS Appl. Mater. Interfaces 16 (2024) 15416–15425, https://doi.org/10.1021/acsami.3c15504.
[8] Z. Huang, W. Zhou, X. Tang, Effects of annealing time on infrared emissivity of the Pt film grown on Ni alloy, Appl. Surf. Sci. 256 (2010) 2025–2030, https://doi.org/10.1016/j.apsusc.2009.09.042.
[9] M.B. Cinali, Ö.D. Coşkun, Optimization of physical properties of sputtered silver films by change of deposition power for low emissivity applications, J. Alloys Compd. 853 (2021) 157073, https://doi.org/10.1016/j.jallcom.2020.157073.
[10] Z. Huang, D. Zhu, F. Lou, W. Zhou, An application of Au thin-film emissivity barrier on Ni alloy, Appl. Surf. Sci. 255 (2008) 2619–2622, https://doi.org/10.1016/j.apsusc.2008.07.185.
[11] L. Wang, Z. Shen, G. Du, P. Wang, P. Wang, The thermal stability of silver-based high reflectance coatings, Thin Solid Films 616 (2016) 122–125, https://doi.org/10.1016/j.tsf.2016.08.013.
[12] M. Fedel, C. Zanella, S. Rossi, F. Deflorian, Corrosion protection of silver coated reflectors by atomic layer deposited Al_2O_3, Sol. Energy 101 (2014) 167–175, https://doi.org/10.1016/j.solener.2013.11.038.
[13] C. Hu, J. Liu, J. Wang, Z. Gu, C. Li, Q. Li, Y. Li, S. Zhang, C. Bi, X. Fan, W. Zheng, New design for highly durable infrared-reflective coatings, Light Sci. Appl. 7 (2018), https://doi.org/10.1038/lsa.2017.175, 17175–17175.
[14] L. Kang, Y. Gao, Z. Chen, J. Du, Z. Zhang, H. Luo, Pt/VO_2 double-layered films combining thermochromic properties with low emissivity, Sol. Energy Mater. Sol. Cells 94 (2010) 2078–2084, https://doi.org/10.1016/j.solmat.2010.06.023.
[15] M. Zhang, M. Li, Z. Yan, L. Zhang, J. Yin, X. Ma, W. Li, L. Deng, Multifunctional Ag-ZrB_2 composite film with low infrared emissivity, low visible light reflectance and hydrophobicity, Appl. Surf. Sci. 604 (2022) 154626, https://doi.org/10.1016/j.apsusc.2022.154626.
[16] W. Zhang, W. Shan, M. Qian, Y. Liu, K. Yu, A Mo/Si multilayer film based selective thermal emitter for high-temperature infrared stealth application, Infrared Phys. Technol. 131 (2023) 104643, https://doi.org/10.1016/j.infrared.2023.104643.
[17] L. Peng, D. Liu, H. Cheng, S. Zhou, M. Zu, A multilayer film based selective thermal emitter for infrared stealth technology, Adv. Opt. Mater. 6 (2018) 1801006, https://doi.org/10.1002/adom.201801006.
[18] W. Xi, Y.-J. Lee, S. Yu, Z. Chen, J. Shiomi, S.K. Kim, R. Hu, Ultrahigh-efficient material informatics inverse design of thermal metamaterials for visible-infrared-compatible camouflage, Nat. Commun. 14 (2023) 4694, https://doi.org/10.1038/s41467-023-40350-6.
[19] D. Ding, X. He, S. Liang, W. Wei, S. Ding, Porous nanostructured composite film for visible-to-infrared camouflage with thermal management, ACS Appl. Mater. Interfaces 14 (2022) 24690–24696, https://doi.org/10.1021/acsami.2c03509.
[20] S. Fang, N. Xu, L. Zhou, T. Wei, Y. Yang, Y. Liu, J. Zhu, Self-assembled skin-like metamaterials for dual-band camouflage, Sci. Adv. 10 (2024) eadl1896, https://doi.org/10.1126/sciadv.adl1896.
[21] K.-T. Lin, H. Lin, T. Yang, B. Jia, Structured graphene metamaterial selective absorbers for high efficiency and omnidirectional solar thermal energy conversion, Nat. Commun. 11 (2020) 1389, https://doi.org/10.1038/s41467-020-15116-z.
[22] H. Li, C. Shen, X. Qiu, S. Zhou, M. Liu, C. Li, H. Zhang, Z. Zhang, Template-made ultrahigh, broadband, and omnidirectional light absorption surface for enhanced solar energy harvesting and utilization, Adv. Funct. Mater. 34 (2024) 2407135, https://doi.org/10.1002/adfm.202407135.

[23] Y. Xiong, Y. Zhou, J. Tian, W. Wang, W. Zhang, D. Zhang, Scalable, color-matched, flexible plasmonic film for visible–infrared compatible camouflage, Adv. Sci. 10 (2023) 2303452, https://doi.org/10.1002/advs.202303452.
[24] Y. Wu, J. Pan, X. Fan, Q. Lu, Y. Gong, X. Huang, K. Chang, T. Wang, J. He, Magnetron sputtering method for the preparation of Cu-ZrB_2 composite film and their optical properties, J. Alloys Compd. 983 (2024) 173850, https://doi.org/10.1016/j.jallcom.2024.173850.
[25] M. Zhang, G. Yang, L. Zhang, Y. Zhang, J. Yin, X. Ma, J. Wen, L. Dai, X. Wang, H. Chen, L. Zhang, L. Yin, X. Jian, X. Zhao, L. Deng, Application of ZrB_2 thin film as a low emissivity film at high temperature, Appl. Surf. Sci. 527 (2020) 146763, https://doi.org/10.1016/j.apsusc.2020.146763.
[26] H. Muñoz, J.E. Antonio, J.M. Cervantes, M. Romero, J.L. Rosas-Huerta, E. P. Arévalo-López, E. Carvajal, R. Escamilla, A first-principles study of the electronic, mechanical, vibrational, and optical properties of the zirconium carbide under high pressure, Phys. Scri. 98 (2023) 025817, https://doi.org/10.1088/1402-4896/acb326.
[27] Y. Dai, F. Zeng, H. Liu, Y. Gao, Q. Yang, M. Chen, R. Huang, Y. Gu, Controlled nitrogen content synthesis of hafnium carbonitride powders by carbonizing hafnium nitride for enhanced ablation properties, Ceram. Int. 49 (2023) 33265–33274, https://doi.org/10.1016/j.ceramint.2023.08.035.
[28] Y. Fu, Y. Zhang, H. Yan, J. Li, X. Yin, J. Sun, Q. Fu, R. Riedel, Microstructure and evolution of hafnium carbide whiskers via polymer-derived ceramics: a novel formation mechanism, J. Adv. Ceram. 12 (2023) 578–586, https://doi.org/10.26599/jac.2023.9220706.
[29] C.J. Smith, X.-X. Yu, Q. Guo, C.R. Weinberger, G.B. Thompson, Phase, hardness, and deformation slip behavior in mixed $Hf_xTa_{1-x}C$, Acta Mater. 145 (2018) 142–153, https://doi.org/10.1016/j.actamat.2017.11.038.
[30] G. Li, G. Li, Microstructure and mechanical properties of hafnium carbide coatings synthesized by reactive magnetron sputtering, J. Coating Technol. Res. 7 (2010) 403–407, https://doi.org/10.1007/s11998-009-9225-x.
[31] W. Shuo, Z. Kan, A. Tao, H. Chaoquan, M. Qingnan, M. Yuanzhi, W. Mao, Z. Weitao, Structure, mechanical and tribological properties of HfC_x films deposited by reactive magnetron sputtering, Appl. Surf. Sci. 327 (2015) 68–76, https://doi.org/10.1016/j.apsusc.2014.11.130.
[32] S.J. Clark, M.D. Segall, C.J. Pickard, P.J. Hasnip, M.I.J. Probert, K. Refson, M. C. Payne, First principles methods using CASTEP, Z. Kristallogr. Cryst. Mater. 220 (2005) 567–570, https://doi.org/10.1524/zkri.220.5.567.65075.
[33] Burke Perdew, Ernzerhof, generalized gradient approximation made simple, Phys. Rev. Lett. 77 (1996) 3865–3868, https://doi.org/10.1103/physrevlett.77.3865.
[34] Vanderbilt, soft self-consistent pseudopotentials in a generalized eigenvalue formalism, Phys. Rev. B Condens. Matter 41 (1990) 7892–7895, https://doi.org/10.1103/physrevb.41.7892.
[35] D.J. Chadi, Special points for Brillouin-zone integrations, Phys. Rev. B 16 (1977) 1746–1747, https://doi.org/10.1103/physrevb.16.1746.
[36] A. Zunger, S.H. Wei, L.G. Ferreira, J.E. Bernard, Special quasirandom structures, Phys. Rev. Lett. 65 (1990) 353–356, https://doi.org/10.1103/physrevlett.65.353.
[37] A. van de Walle, P. Tiwary, M. de Jong, D.L. Olmsted, M. Asta, A. Dick, D. Shin, Y. Wang, L.Q. Chen, Z.K. Liu, Efficient stochastic generation of special quasirandom structures, Calphad 42 (2013) 13–18, https://doi.org/10.1016/j.calphad.2013.06.006.
[38] P. Fang, C.P. Mulligan, R. Jia, J. Shi, S.V. Khare, D. Gall, Epitaxial TiC_x (001) layers: phase formation and physical properties *vs* C-to-Ti ratio, Acta Mater. 226 (2022) 117643, https://doi.org/10.1016/j.actamat.2022.117643.
[39] A. Anders, A structure zone diagram including plasma-based deposition and ion etching, Thin Solid Films 518 (2010) 4087–4090, https://doi.org/10.1016/j.tsf.2009.10.145.
[40] W. Yang, J. Shen, Z. Wang, G. Ma, P. Ke, A. Wang, Mechanical and electrochemical properties of $(MoNbTaTiZr)_{1-x}N_x$ high-entropy nitride coatings, J. Mater. Sci. Technol. 208 (2025) 78–91, https://doi.org/10.1016/j.jmst.2024.04.062.
[41] H.S. Seo, T. Lee, H. Kim, I. Petrov, J.E. Greene, Phase composition of polycrystalline HfN_x ($0.45 \leq x \leq 1.60$) and effects of low-energy ion irradiation on microstructure, texture, and physical properties, J. Vac. Sci. Technol. A 41 (2023) 063406, https://doi.org/10.1116/6.0003072.
[42] A.L. Vyatskikh, B.E. MacDonald, A.D. Dupuy, E.J. Lavernia, J.M. Schoenung, H. Hahn, High entropy silicides: CALPHAD-Guided prediction and thin film fabrication, Scr. Mater. 201 (2021) 113914, https://doi.org/10.1016/j.scriptamat.2021.113914.
[43] J. Hu, H. Li, J. Li, Q. Wu, J. Huang, J. Kong, Y. Shi, G. Zhang, D. Xiong, Effect of Ag target power on structure, mechanical properties of TaC–Ag films, Ceram. Int. 48 (2022) 11718–11728, https://doi.org/10.1016/j.ceramint.2022.01.030.
[44] J. Hu, H. Li, J. Li, C. Yan, J. Kong, Q. Wu, D. Xiong, Super-hard and tough $Ta_{1-x}W_xC_y$ films deposited by magnetron sputtering, Surf. Coating. Technol. 400 (2020) 126207, https://doi.org/10.1016/j.surfcoat.2020.126207.
[45] Z. Gu, C. Hu, X. Fan, L. Xu, M. Wen, Q. Meng, L. Zhao, X. Zheng, W. Zheng, On the nature of point defect and its effect on electronic structure of rocksalt hafnium nitride films, Acta Mater. 81 (2014) 315–325, https://doi.org/10.1016/j.actamat.2014.08.040.
[46] M.D. Hossain, T. Borman, A. Kumar, X. Chen, A. Khosravani, S.R. Kalidindi, E. A. Paisley, M. Esters, C. Oses, C. Toher, S. Curtarolo, J.M. LeBeau, D. Brenner, J. P. Maria, Carbon stoichiometry and mechanical properties of high entropy carbides, Acta Mater. 215 (2021) 117051, https://doi.org/10.1016/j.actamat.2021.117051.
[47] H. Lasfargues, T. Glechner, C.M. Koller, V. Paneta, D. Primetzhofer, S. Kolozsvári, D. Holec, H. Riedl, P.H. Mayrhofer, Non-reactively sputtered ultra-high temperature Hf-C and Ta-C coatings, Surf. Coat. Technol. 309 (2017) 436–444, https://doi.org/10.1016/j.surfcoat.2016.11.073.
[48] X. Chai, D. Zhu, Y. Liu, Y. Qing, Z. Ren, F. Luo, W. Zhou, Z. Huang, P. Li, Silver-modified chromium(III) oxide as multi-band compatible stealth materials for visual/infrared stealth and radar wave transmission, Compos. Sci. Technol. 216 (2021) 109038, https://doi.org/10.1016/j.compscitech.2021.109038.
[49] L. Yuan, J. Hu, X. Weng, Q. Zhang, L. Deng, Galvanic displacement synthesis of Al/Ni core–shell pigments and their low infrared emissivity application, J. Alloys Compd. 670 (2016) 275–280, https://doi.org/10.1016/j.jallcom.2016.02.028.
[50] Y. Liu, J. Xie, M. Luo, S. Jian, B. Peng, L. Deng, The synthesis and characterization of Al/Co_3O_4 magnetic composite pigments with low infrared emissivity and low lightness, Infrared Phys. Technol. 83 (2017) 88–93, https://doi.org/10.1016/j.infrared.2017.04.014.
[51] L. Yuan, X. Weng, J. Xie, W. Du, L. Deng, Solvothermal synthesis and visible/infrared optical properties of Al/Fe_3O_4 core–shell magnetic composite pigments, J. Alloys Compd. 580 (2013) 108–113, https://doi.org/10.1016/j.jallcom.2013.05.100.
[52] Y. Liu, J. Xie, M. Luo, B. Peng, C. Xu, L. Deng, The synthesis and optical properties of Al/MnO_2 composite pigments by ball-milling for low infrared emissivity and low lightness, Prog. Org. Coating 108 (2017) 30–35, https://doi.org/10.1016/j.porgcoat.2017.03.019.
[53] K. Wang, C. Wang, Y. Yin, K. Chen, Modification of Al pigment with graphene for infrared/visual stealth compatible fabric coating, J. Alloys Compd. 690 (2017) 741–748, https://doi.org/10.1016/j.jallcom.2016.08.171.
[54] A. Rana, N.K. Sharma, S. Bera, A. Yadav, G. Gupta, A.S. Rana, Tuning the plasmonic resonance in TiN refractory metal, Sci. Rep. 14 (2024) 7905, https://doi.org/10.1038/s41598-024-55000-0.
[55] W.P. Guo, R. Mishra, C.W. Cheng, B.H. Wu, L.J. Chen, M.T. Lin, S. Gwo, Titanium nitride epitaxial films as a plasmonic material platform: alternative to gold, ACS Photonics 6 (2019) 1848–1854, https://doi.org/10.1021/acsphotonics.9b00617.
[56] S. Saha, M.G. Ozlu, S.N. Chowdhury, B.T. Diroll, R.D. Schaller, A. Kildishev, A. Boltasseva, V.M. Shalaev, Tailoring the thickness-dependent optical properties of conducting nitrides and oxides for epsilon-near-zero-enhanced photonic applications, Adv. Mater. 35 (2023) e2109546, https://doi.org/10.1002/adma.202109546.
[57] O.A. Tertuliano, P.J. DePond, A.C. Lee, J. Hong, D. Doan, L. Capaldi, M. Brongersma, X.W. Gu, M.J. Matthews, W. Cai, A.J. Lew, High absorptivity nanotextured powders for additive manufacturing, Sci. Adv. 10 (2024) eadp0003, https://doi.org/10.1126/sciadv.adp0003.
[58] Y. Li, C. Xiong, H. Huang, X. Peng, D. Mei, M. Li, G. Liu, M. Wu, T. Zhao, B. Huang, 2D $Ti_3C_2T_x$ MXenes: Visible black but infrared white materials, Adv. Mater. 33 (2021) e2103054, https://doi.org/10.1002/adma.202103054.
[59] P. Ren, M. Wen, K. Zhang, S. Du, Y. Zhang, J. Chen, W. Zheng, Self-assembly of TaC@Ta core–shell-like nanocomposite film via solid-state dewetting: toward superior wear and corrosion resistance, Acta Mater. 160 (2018) 72–84, https://doi.org/10.1016/j.actamat.2018.08.055.
[60] C.H. Yeh, W.D. Hsu, B.H. Liu, C.S. Yang, C.Y. Kuan, Y.C. Chang, K.S. Huang, S. S. Jhang, C.Y. Lu, P.K. Liaw, C.F. Shih, Low-frequency conductivity of low wear high-entropy alloys, Nat. Commun. 15 (2024) 4554, https://doi.org/10.1038/s41467-024-49035-0.
[61] Y.T. Li, X.M. Chen, X.K. Zeng, M. Liu, X. Jiang, Y.X. Leng, Hard yet tough and self-lubricating $(CuNiTiNbCr)C_x$ high-entropy nanocomposite films: effects of carbon content on structure and properties, J. Mater. Sci. Technol. 173 (2024) 20–30, https://doi.org/10.1016/j.jmst.2023.05.082.